NUMERICAL SIMULATION OF CAPILLARY-CONTROLLED THREE-PHASE DISPLACEMENTS ON 3D ROCK IMAGES

Johan Olav Helland and Espen Jettestuen
IRIS – International Research Institute of Stavanger, Stavanger, Norway

This paper was prepared for presentation at the International Symposium of the Society of Core Analysts held in Avignon, France, 8-11 September, 2014

ABSTRACT

We simulate three-phase capillary-controlled displacement using a multiphase variational level set method which is extended to account for the presence of a static solid phase and arbitrary, uniform contact angles. Motion of gas/oil/water triple lines is captured very well with the method, whereas oil layers require high resolution to be modelled accurately. We validate the method and apply it to simulate gas invasion and simultaneous water- and gas-invasions after primary drainage on small, water-wet sandstone geometry. The three-phase gas/oil and oil/water capillary pressure curves are relatively similar to the corresponding two-phase curves, but they show some differences that can be explained by pore-scale mechanisms. During gas invasion into oil and water, existing water layers in pore corners affect the gas/oil capillary entry pressures in parts of the sandstone geometry, whereas narrow water-filled throats prohibit invasion of gas which instead displaces oil in other locations. During water invasion in the three-phase case, water snap-off occurs frequently on gas/oil interfaces due to growth of water cusps at gas/oil/solid contact lines. This mechanism is observed to occur at a higher oil/water capillary pressure than the standard two-phase snap-off events in which cusps are absent.

INTRODUCTION

Three-phase enhanced oil recovery methods, such as depressurization, gas drainage and water-alternate-gas (WAG) injection, require reliable models for three-phase capillary pressure and relative permeability, hysteresis and phase trapping. However, measuring three-phase capillary pressure is extremely time-consuming and challenging [16], and few three-phase hysteresis data exist. Therefore, the common practice is to describe three-phase capillary pressure and relative permeability in terms of correlations that are based on much more readily available two-phase data. However, several studies show that this approach may not describe the three-phase flow properties with sufficient accuracy [7, 13]. Most three-phase hysteresis models are developed for relative permeability, but reservoir-simulation results of WAG injection depend on the hysteresis model used [11]. Further, three-phase trapping models [5] should account for the large variations of residual gas and oil saturations observed in core-scale water floods [2].

Pore-scale modelling can be applied to determine consistent flow properties, including hysteresis and phase-trapping behaviour, by simulating the fluid distribution directly in

porous rocks. Among existing computational approaches [1, 4, 10, 15], network modelling [1] is currently the most developed method for three-phase flow and previous studies identify oil layers and multiple displacement events as key mechanisms that control residual oil [1]. Since network models represent the porous structure as connected pore elements of idealized shapes, high-resolution numerical simulations performed directly on 3D rock images should result in a more realistic three-fluid distribution and oil-layer structure. Thus far, only 2D lattice-Boltzmann models [15] have been used to simulate three-phase flow in arbitrary pore geometries to our knowledge.

The Level Set (LS) method [9] describes fluid interfaces implicitly as the zero contours of a scalar function and can handle changes of interface topology in a natural manner. The Variational Level Set (VLS) method proposed by Zhao *et al*. [17] is an extension of the LS method for modelling the motion of three fluids and is capable of describing the evolution of triple junctions in three-fluid systems very well. Other variational methods for triple-junction motion are proposed more recently [3, 12]. However, none of these methods incorporate a solid phase. Recently, we extended the conventional LS method [10] to allow for nonzero contact angles on the solid surface [4]. In this work, we present a similar extension of the VLS method [17] which enables us to simulate three-fluid displacements in porous media with arbitrary, yet uniform wettability. As a first step, we validate the method on idealized geometries and then simulate three-phase capillary pressure curves for gas invasion and simultaneous water- and gas-invasion (SWAG) processes directly on a 3D segmented image subset of sandstone geometry.

MULTIPHASE FLUID-SOLID VLS METHOD

We shall develop a numerical method which simulates capillary-controlled three-phase displacements at the pore scale. Thus, at equilibrium, the interfaces satisfy Young-Laplace equation in the pore space and Young's equation at the pore/solid boundary:

$$P_{cij} = \sigma_{ij} C_{ij} \quad (1) \qquad \text{and} \qquad \sigma_{ij} \cos\theta_{ij} = \sigma_{is} - \sigma_{js}, \quad ij = go, ow, gw. \quad (2)$$

In these equations, C_{ij} are fluid/fluid interface curvatures, σ_{ij} and σ_{is} are fluid/fluid and fluid/solid interfacial tensions, and θ_{ij} are contact angles. From equation (2) it follows that the contact angles and interfacial tensions in a three-phase system are related by [13]

$$\sigma_{gw} \cos\theta_{gw} = \sigma_{go} \cos\theta_{go} + \sigma_{ow} \cos\theta_{ow}. \quad (3)$$

We adopt van Dijke and Sorbie's linear relationships [13], which satisfy equation (3) and describe $\cos\theta_{gw}$ and $\cos\theta_{go}$ as functions of $\cos\theta_{ow}$, to determine the three-phase contact angles used in this work.

The LS method [9] is a sub-grid-scale interface tracking method which describes fluid interfaces implicitly as the zero contours of a scalar function $\phi(\vec{x})$. Thus, $\phi < 0$ inside the fluid, $\phi > 0$ outside, and $\phi = 0$ on the interfaces. The unit normal vector and curvature is given as $\vec{n}_\phi = \nabla\phi / |\nabla\phi|$ and $\kappa_\phi = \nabla \cdot \vec{n}_\phi$, respectively. The ϕ-fields evolve according to

$$\phi_t + V_n|\nabla\phi| + \vec{V}_{adv}\cdot\nabla\phi = 0, \tag{4}$$

where V_n and $\vec{V}_{adv}$ are normal and advective velocity components. Prodanović and Bryant [10] applied the LS method to simulate two-phase, zero contact angle, capillary-controlled displacement on 3D porous structures, assuming $V_n = C_{ow} - \kappa$ and $\vec{V}_{adv} = \vec{0}$. The solid surfaces are represented by the zero contours of a static LS function ψ. Jettestuen *et al*. [4] included arbitrary contact angles by allowing ϕ to intersect the solid phase. The intersection angle β is related to the fluid/fluid and pore/solid LS contours through the scalar product of their unit normal vectors:

$$\vec{n}_\phi \cdot \vec{n}_\psi = \cos\beta \quad \Leftrightarrow \quad \nabla\phi\cdot\nabla\psi - \cos\beta|\nabla\phi\|\nabla\psi| = 0\,. \tag{5}$$

The contact angle is $\theta = 180^\circ - \beta$. This method introduces different velocities of ϕ in the pore and solid. At equilibrium, $C_{ow} = \kappa$ in pore and equation (5) is satisfied in solid.

Contrary to the LS method, the VLS method by Zhao *et al*. [17] specifies one LS function ϕ_i per fluid. Each fluid is also equipped with a phase pressure p_i and a "surface" tension γ_i. We extend the method to account for a solid phase by also assigning a solid/fluid intersection angle β_i to each fluid such that the zero contours of ϕ_i can intersect the solid. We choose to measure β_i on the interior side of its fluid, see Figure 1. The pore-space domains occupied by the different fluids are given by

$$\Omega_i = \{\vec{x}\in\Omega : \phi_i(\vec{x}) < 0 \text{ and } \psi(\vec{x}) > 0\}, \quad i = g, o, w. \tag{6}$$

Figure 1 illustrates these regions and the parameters introduced in the VLS method.

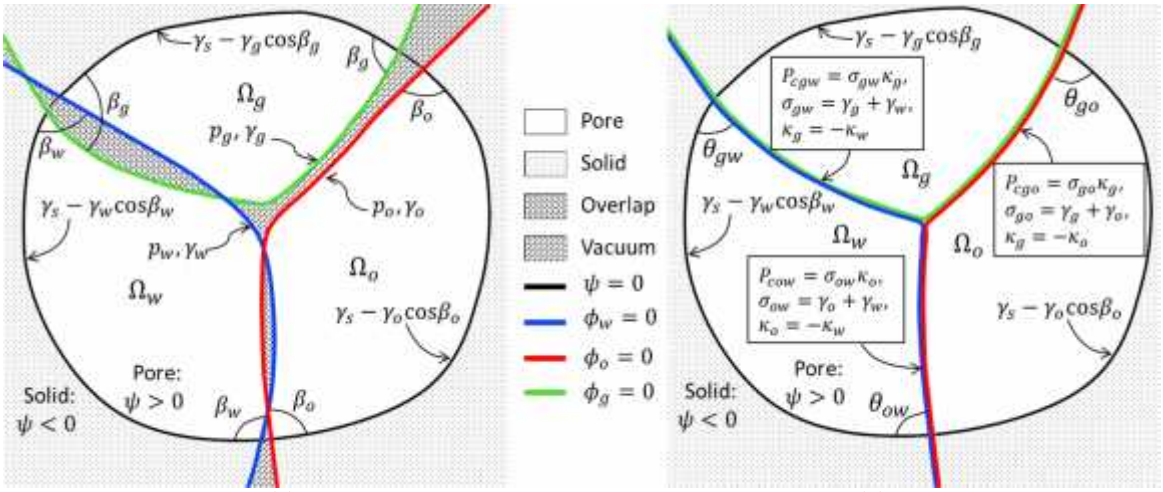

Figure 1: Illustration of the VLS method and its parameters in a simple pore/solid geometry. Figure (a) shows that overlap and/or vacuum regions generally occur if different LS functions move with independent velocities. Figure (b) illustrates the effect of including the no-vacuum/overlap constraint and shows an equilibrium configuration in which Young-Laplace equation is satisfied in the pore space, whereas the contact angles form at the interfaces intersecting the pore walls.

Volume and area quantities are easily calculated by means of Heaviside step functions $H(\ldots)$ and delta functions $\delta(\ldots)$ within the LS framework [9]. Thus, the total energy of the system, which constitutes the sum of bulk fluid, fluid/fluid and solid/fluid interfacial energy, is given by

$$\begin{aligned} E = & \sum_{i=g,o,w} p_i \int_\Omega H(-\phi_i) H(\psi) dV + \sum_{i=g,o,w} \gamma_i \int_\Omega \delta(\phi_i) |\nabla \phi_i| H(\psi) dV \\ & + \sum_{i=g,o,w} (\gamma_s - \gamma_i \cos\beta_i) \int_\Omega H(-\phi_i) \delta(\psi) |\nabla \psi| dV \end{aligned} . \tag{7}$$

The first two terms follow [17], but we add the last term to include the solid/fluid energy. In this description, we express solid/fluid interfacial tensions in terms of the surface tensions and intersection angles as

$$\sigma_{is} = \gamma_s - \gamma_i \cos\beta_i, \quad i = g, o, w. \tag{8}$$

Depending on β_i, the last term in equation (8) can be positive or negative, and the role of the positive constant γ_s is only to ensure $\sigma_{is} > 0$. The term involving γ_s in equation (7) vanishes during minimization of energy as it does not depend on the fluids.

Vacuum or overlap regions may form at the interfaces if the zero contours of ϕ_i move with independent velocities, see Figure 1a. We follow [17] and introduce a constraint which prevents these regions such that $\phi_i = 0$ of the three fluids stay closely aligned:

$$\frac{1}{2} \int_\Omega \left(\sum_{i=g,o,w} H(-\phi_i) - 1 \right)^2 dV = 0. \tag{9}$$

Thus, under action of the constraint, fluid/fluid interfaces appear as the zero contours of the two fluids forming the interface, see Figure 1b. This gives rise to interfacial tensions on the interfaces, which are defined as

$$\sigma_{ij} = \gamma_i + \gamma_j, \quad ij = go, ow, gw, \tag{10}$$

and contact angles at the interface-solid intersections, which satisfy

$$(\gamma_i + \gamma_j) \cos\theta_{ij} = \gamma_j \cos\beta_j - \gamma_i \cos\beta_i, \quad \text{for } ij = go, ow, gw, \tag{11}$$

in equilibrium. Equation (11) is equivalent to Young's equation (2). Consequently, equations (10) and (11) are consistent with equation (3). Applying the linear contact angle relations [13], it follows that $\beta_w = \theta_{ow}$, $\beta_o = 180^\circ - \theta_{ow}$ and $\beta_g = 180^\circ$.

In equation (7), we replace $\delta(\psi)$ with $H(\psi)/\Delta x$ to extend contact angle formation into solid, following [4]. Numerically, this describes the contact angle on the pore/solid surface more accurately. The intersection angle must satisfy equation (5). Thus, we propose to minimize the following functional to account for all features:

$$\begin{aligned} f(\phi_g, \phi_o, \phi_w) = \int_\Omega \Bigg(& \sum_{i=g,o,w} p_i H(-\phi_i) H(\psi) + \sum_{i=g,o,w} \gamma_i \delta(\phi_i) |\nabla \phi_i| H(\psi) + \frac{\lambda}{2} \left(\sum_{j=g,o,w} H(-\phi_j) - 1 \right)^2 \\ & - \sum_{i=g,o,w} \gamma_i \left(\frac{\nabla \phi_i}{|\nabla \phi_i|} \cdot \frac{\nabla \psi}{|\nabla \psi|} - \cos\beta_i \right) \frac{H(-\psi)}{\Delta x} |\nabla \psi| H(-\phi_i) \Bigg) dV. \end{aligned} \tag{12}$$

The first three terms on the right-hand side of equation (12) follow [17], whereas the last term is responsible for forming the contact angle on the pore wall and extend it into solid. λ is a Lagrange multiplier. Minimizing equation (12) amounts to calculating the Frechét derivative of *f* with respect to ϕ_i, and determining the solutions $\partial f / \partial \phi_i = 0$, $i = g, o, w$. Following [17], we find that the evolution equations are given by

$$\begin{aligned}(\phi_i)_t + H(\psi)(p_i - \gamma_i \kappa_i)|\nabla \phi_i| + \lambda\left(\sum_{j=g,o,w} H(-\phi_j) - 1\right)|\nabla \phi_i| \\ + H(-\psi)S(\psi)\frac{\gamma_i}{\Delta x}\left(\nabla \phi_i \cdot \nabla \psi - \cos\beta_i |\nabla \phi_i||\nabla \psi|\right) = 0, \quad i = g, o, w,\end{aligned} \tag{13}$$

with boundary conditions on the computational domain given by $\vec{n} \cdot \nabla \phi_i = 0$ for *i=g,o,w*. In equation (13) we added a smooth sign function $S(\psi)$ to ensure numerical stability [4]. The three evolution equations (13) are coupled only through the constraint and the Lagrange multiplier λ which is given by

$$\lambda = \frac{\begin{aligned}\sum_{i=g,o,w} \int_\Omega \left(\sum_{j=g,o,w} H(-\phi_j) - 1\right)\delta(\phi_i)\Big(H(\psi)(\gamma_i \kappa_i - p_i)|\nabla \phi_i| + \\ H(-\psi)S(\psi)\frac{\gamma_i}{\Delta x}\left(\cos\beta_i |\nabla \phi_i||\nabla \psi| - \nabla \phi_i \cdot \nabla \psi\right)\Big) dV\end{aligned}}{\sum_{i=g,o,w} \int_\Omega \left(\sum_{j=g,o,w} H(-\phi_j) - 1\right)^2 \delta(\phi_i)|\nabla \phi_i| dV}. \tag{14}$$

It follows from the evolution equations (13) that an interface between fluid *i* and *j* obtains equilibrium in the pore space if

$$(p_i - \gamma_i \kappa_i)|\nabla \phi_i| = (p_j - \gamma_j \kappa_j)|\nabla \phi_j|. \tag{15}$$

Because the interfacial tension is given by equation (10), $|\nabla \phi_i| = |\nabla \phi_j|$ and $C_{ij} = \kappa_i = -\kappa_j$ is satisfied on the interface, we recover Young-Laplace's equation (1). Similarly, equilibrium is reached along an *ij* -interface intersecting the solid phase if

$$\gamma_i(\nabla \phi_i \cdot \nabla \psi - \cos\beta_i |\nabla \phi_i||\nabla \psi|) = \gamma_j(\nabla \phi_j \cdot \nabla \psi - \cos\beta_j |\nabla \phi_j||\nabla \psi|). \tag{16}$$

Because $\nabla \phi_i = -\nabla \phi_j$ at the interface, and $\vec{n}_{\phi_j} \cdot \vec{n}_\psi = \cos\theta_{ij}$, we obtain equation (11).

The evolution equations (13) are solved by standard explicit numerical schemes for LS methods [9, 4]. For non-wetting phase invasion we add, to the inlet face, a pore-space layer occupied by invading phase, while for invasion of wetting or intermediate-wetting phases, we instead add a porous plate saturated and wetted by the invading phase.

SIMULATION RESULTS

The input parameters for the VLS method are phase pressures p_i, surface tensions γ_i and intersection angles β_i for all fluids. For a given set of three-phase interfacial tensions and contact angles [13], we use equations (10) and (11) to determine the corresponding γ_i

and β_i. Table 1 shows the parameter combinations applied in this work. We use the VLS method to simulate three-phase processes quasi-statically by changing the phase pressures stepwise, and in each step, we solve equations (13) and (14) until equilibrium states are reached and fluid saturations are calculated. The two-phase saturation history is simulated with the contact-angle LS method [4] which describes interfaces by one LS function and is thus less computationally expensive. We use voxel length $\Delta x^{sim} = 0.001$ in all simulations. The results are plotted in terms of physical interface curvature $C_{ij} = P_{cij}^{sim} \Delta x^{sim} / (\sigma_{ij}^{sim} \Delta x), ij = go, ow, gw$, where Δx is physical voxel length. We visualize fluid interfaces inside the pore space as iso-surfaces $\phi_i = 0$ of $\phi_i = \min(-\phi_i, \psi), i = g, o, w$.

	Physical parameters						Model parameters					
Case	σ_{ow} (N/m)	σ_{go} (N/m)	σ_{gw} (N/m)	θ_{ow} (deg)	θ_{go} (deg)	θ_{gw} (deg)	γ_w (N/m)	γ_o (N/m)	γ_g (N/m)	β_w (deg)	β_o (deg)	β_g (deg)
1	**0.02**	**0.0101**	**0.03**	**40**	**7.6**	**32.4**	**1.995**	**0.005**	**1.005**	**40**	**140**	**180**
2	**0.02**	**0.0101**	**0.03**	**20**	**7.9**	**16.3**	**1.995**	**0.005**	**1.005**	**20**	**160**	**180**
3	**0.02**	**0.005**	**0.023**	**40**	**49.7**	**36.2**	**1.9**	**0.1**	**0.4**	**40**	**140**	**180**

Table 1: Parameters for the physical systems and corresponding model systems used in the simulations. All simulations were carried out using $\Delta x^{sim} = 0.001$. The model interfacial tensions ($\gamma_i + \gamma_j$) are rescaled such that all $\gamma_i > \Delta x^{sim}$ [17]. The phase pressures given as input are increased correspondingly.

Validation. We validate the three-phase VLS method by comparing simulations against analytical three-phase solutions in idealized 3D pore geometries. First, we consider gas invasion into a straight tube with star-shaped cross-section initially occupied by oil in the bulk portion and water in the corners, using Case 1 parameters (see Table 1). Results are shown in Figure 2. Simulated gas-oil entry curvature agrees well with the analytical curvature calculated by Mayer & Stowe-Princen (MS-P) method (e.g., [8]), and the relative error is less than 5.9 %. Consistent with the three-phase extension of the MS-P method [14], oil layers form between bulk gas and corner water. According to analytical calculations [14], oil layers should exist up to $C_{go} = 0.37\ \mu m^{-1}$. However, in the VLS simulation, oil-layer displacements occur at smaller and different gas-oil curvatures, and all layers are displaced at $C_{go} = 0.28\ \mu m^{-1}$. A more accurate description of the oil-layer existence requires higher grid resolution.

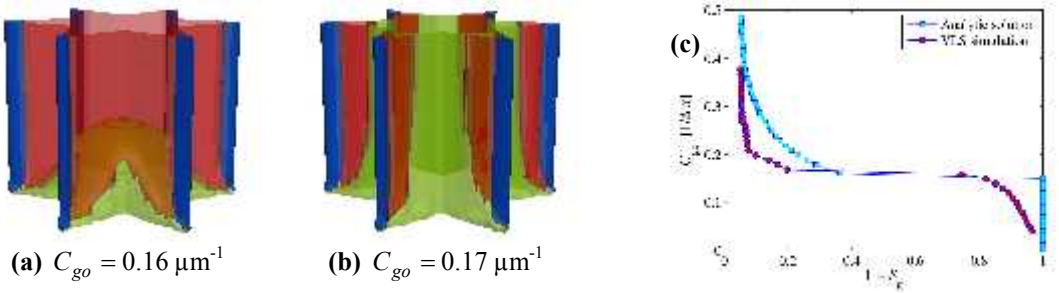

(a) $C_{go} = 0.16\ \mu m^{-1}$ **(b)** $C_{go} = 0.17\ \mu m^{-1}$

Figure 2: Stable configurations of gas (green), oil (red) and water (blue) (a, b) during upward gas invasion into a straight tube with constant star-shape cross-section, using Case 1 parameters and physical voxel length $\Delta x = 1\ \mu m$. Gas invasion is simulated at constant oil-water interface curvature $C_{ow} = 0.24\ \mu m^{-1}$. Figure (c) compares the simulated curvature-saturation curve against analytical three-phase results [14].

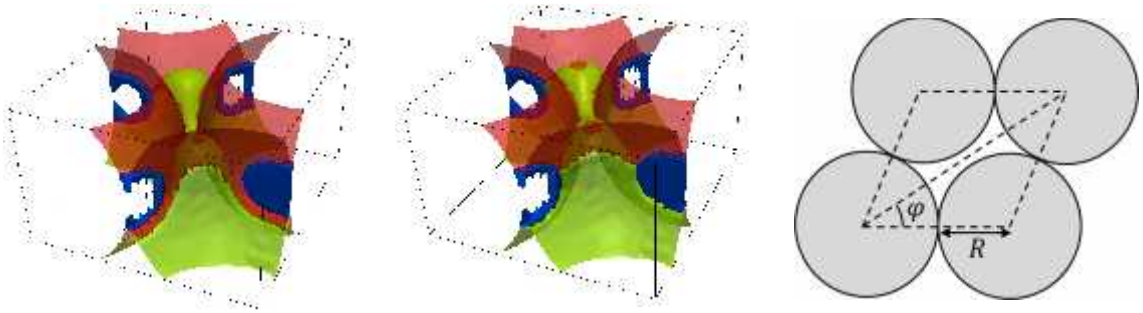

(a) $C_{go} = 0.327\ \mu m^{-1}$ **(b)** $C_{go} = 0.28\ \mu m^{-1}$ **(c)**

Figure 3: Fluid configurations of gas (green), oil (red) and water (blue) during gas invasion into a sphere-pack pore throat, using physical voxel length $\Delta x = 1$ µm, Case 2 (a) and Case 3 (b) parameters. The pore geometry (c) is initially occupied by bulk oil and water rings that are located around the sphere contacts. Gas invasion is simulated at constant oil-water curvatures $C_{ow} = 0.5\ \mu m^{-1}$ (a) and $C_{ow} = 0.32\ \mu m^{-1}$ (b).

Similar gas invasions are simulated in a pore throat formed by the space between four spheres with half angle $\varphi = 32^\circ$ and radius $R = 30$ µm as shown in Figure 3, using Case 2 and 3 parameters. Two-phase oil-water entry curvatures are calculated by the contact-angle LS method [4], and in Case 2, dimensionless oil-water entry curvature is $C_{ow}R = 9.0$ while the analytical value obtained from two-phase MS-P/Purcell method (Table 2 in [8]) is 9.4, which gives a relative error of 4.2%. The following gas invasions are simulated with VLS method. In Case 2 (Figure 3a), oil layers exist in the last stable configuration before gas invades the throat. Thus, the three-phase gas-oil entry curvature is most likely not influenced by the water rings and is similar to the equivalent two-phase curvature. We obtain entry curvature $9.51 < C_{go}R < 9.81$, while two-phase MS-P/Purcell method (with $\theta_{go} = 10^\circ$) gives 9.65. Thus, the relative error is smaller than 3.1%.

In Case 3 (Figure 3b), almost all oil layers have collapsed in the last stable configuration before gas invasion, and gas/oil/water triple lines form. Consequently, the gas-oil entry curvature depends on the water pressure. In this case, we obtain $7.8 < C_{go}R < 8.4$, while the two-phase MS-P/Purcell method gives 7.48, resulting in a relative error less than 10.9%. The larger deviation in this case might be due to the impact of the water rings. We also applied the three-phase MS-P method [14] on an equivalent straight tube formed by the space between four cylinders with radii $R = 30$ µm and $\varphi = 32^\circ$ and found only minor differences when compared with the standard two-phase MS-P method (Table 1 in [8]). However, the difference between two- and three-phase entry curvatures in sphere-pack throats is not known and could show different behaviour than in cylindrical throats. The MS-P/Purcell method is more accurate than the standard MS-P method in sphere-pack throats, particularly for large contact angles, but it is valid for two phases only.

Sandstone pore structures. We extracted a small subset of size 60x60x70 voxels from a freely available, segmented 3D image of Castlegate sandstone with voxel length $\Delta x = 5.6$ µm. From two initial water saturations S_{wi} after primary drainage, we simulate water

imbibition and three-phase gas- and SWAG-invasion processes on the extracted subset using Case 2 parameters. The two-phase processes are simulated with contact-angle LS method [4]. Three-phase gas invasion is simulated by increasing gas pressure stepwise using bottom face as inlet, while the other phase pressures are constant. SWAG invasions are performed similarly, except that gas and water pressures are increased stepwise at the same time. The water pressure is increased by twice the gas-pressure increment.

Figure 4 presents the simulated results. For the SWAG process at $S_{wi} = 0.13$, we plot in Figure 4b only the branch of the gas-oil curve that corresponds to increasing gas saturation in the displacement path shown in Figure 4a. Overall, the two- and three-phase curvature curves are similar, which is as expected at water-wet conditions [6]. However, some deviations in the gas-oil curvature curves occur at liquid saturations smaller than 0.7, see Figure 4b. The two-phase oil-water primary drainage curve is slightly higher than the three-phase gas-oil curves despite $\theta_{go} < \theta_{ow}$. We explain this by the presence of water films, which, depending on geometry and water pressure, can result in smaller gas-oil entry curvatures [14]. However, at increased S_{wi}, narrow throats can be occupied by water, and gas displaces oil at other locations instead. This results in higher levels of the gas-oil curvature curves, as shown in Figure 4b. In the SWAG processes, water snap-off occurs as a result of water-cusp growth at the gas/oil/solid contact lines, which causes gas and oil to retract to wider pore openings while water occupies the narrower throats. This reduces the possible paths for gas/oil displacements. Further, growth of water layers during SWAG processes may affect the gas/oil capillary entry curvature differently in different locations. Overall, we observe higher gas/oil curvature curves for the SWAG processes, as shown in Figure 4b. Figure 5 shows configurations during gas invasion from $S_{wi} = 0.06$. The gas configurations are similar to the oil configurations in primary drainage. In the three-phase case, oil is isolated in places where water was isolated in primary drainage. These images also show a narrow throat, initially occupied by oil with a gas/oil interface present at its entrance, which gets invaded by water because water cusps at the gas/oil/solid contact lines bridge across the throat. The gas invasion from $S_{wi} = 0.13$ (not shown) exhibit similar trends, but thicker water layers occur and a few narrow constrictions occupied by oil at $S_{wi} = 0.06$ are instead occupied by water.

The two- and three-phase oil-water curvature-saturation curves are shown in Figure 4c. They are relatively similar, which is in agreement with experimental work [6], but parts of the three-phase curves for the SWAG processes are located at higher capillary levels. This is due to three-phase water snap-off mechanisms which we observe to occur frequently as a result of water-cusp growth at gas/oil/solid contact lines. Bridging of water cusps across narrow throats occur at higher oil-water capillary pressures than the snap-off events observed in the corresponding two-phase imbibition simulations. This is because cusp heights can be larger than film thicknesses. Further, water cusps can also affect the film thickness in their vicinity. Water-cusp volume also contributes to higher water saturation than in the two-phase case where cusps are absent. Depending on

geometry, this can also cause water to snap off oil in three-phase systems in the same manner as in the two-phase case, but at higher capillary pressure due to thicker water films in the cusp vicinity. Once the water snap-off mechanisms have separated the gas and oil phase, the three-phase imbibition curve becomes lower than the two-phase curves because a lower capillary pressure is required to displace the gas.

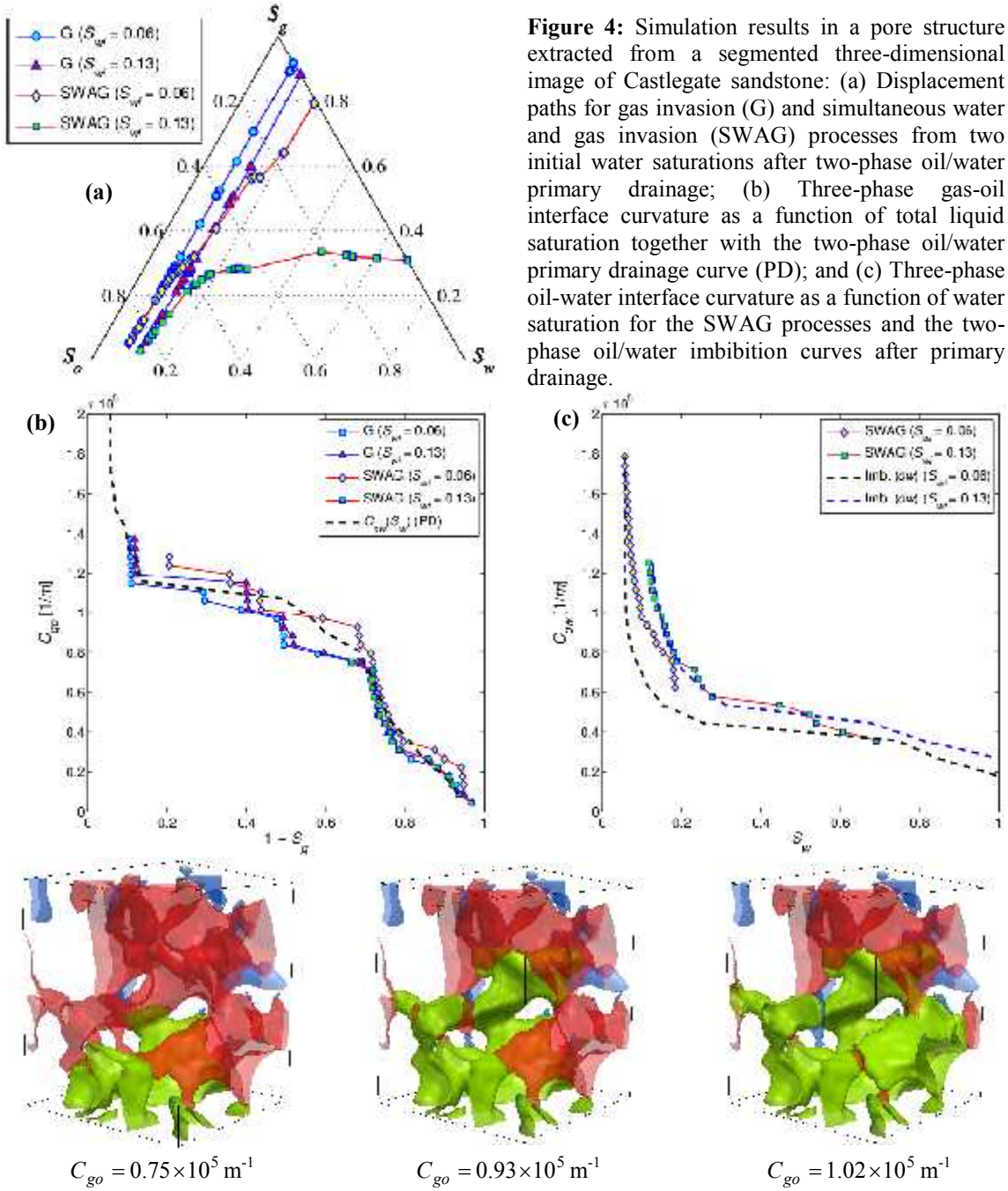

Figure 4: Simulation results in a pore structure extracted from a segmented three-dimensional image of Castlegate sandstone: (a) Displacement paths for gas invasion (G) and simultaneous water and gas invasion (SWAG) processes from two initial water saturations after two-phase oil/water primary drainage; (b) Three-phase gas-oil interface curvature as a function of total liquid saturation together with the two-phase oil/water primary drainage curve (PD); and (c) Three-phase oil-water interface curvature as a function of water saturation for the SWAG processes and the two-phase oil/water imbibition curves after primary drainage.

Figure 5: Stable fluid configurations of gas (green), oil (red) and water (blue) in Castlegate sandstone during gas invasion at constant oil-water capillary pressure from $S_{wi} = 0.06$ after primary drainage.

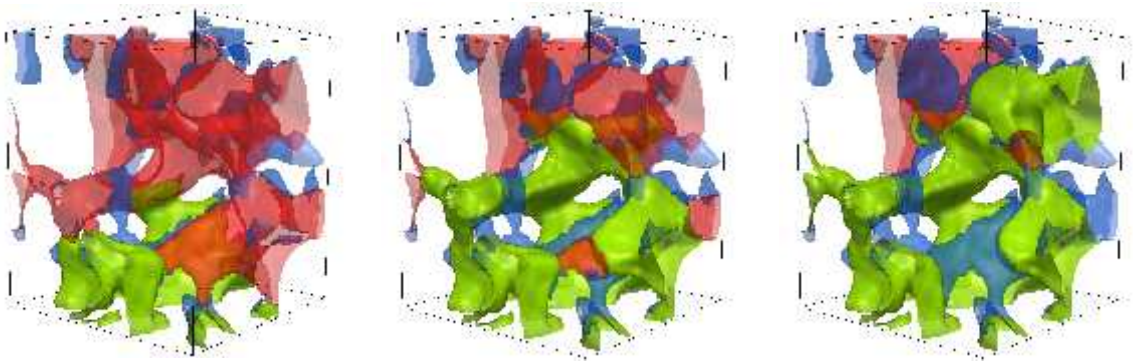

(a) $C_{go} = 0.93\times10^{5}$ m^{-1} $C_{ow} = 0.98\times10^{5}$ m^{-1} **(b)** $C_{go} = 1.02\times10^{5}$ m^{-1} $C_{ow} = 0.89\times10^{5}$ m^{-1} **(c)** $C_{go} = 1.19\times10^{5}$ m^{-1} $C_{ow} = 0.71\times10^{5}$ m^{-1}

Figure 6: Stable three-phase configurations of gas (green), oil (red) and water (blue) in Castlegate sandstone for three combinations of gas-oil and oil-water capillary pressures during SWAG invasion from $S_{wi} = 0.06$ after primary drainage.

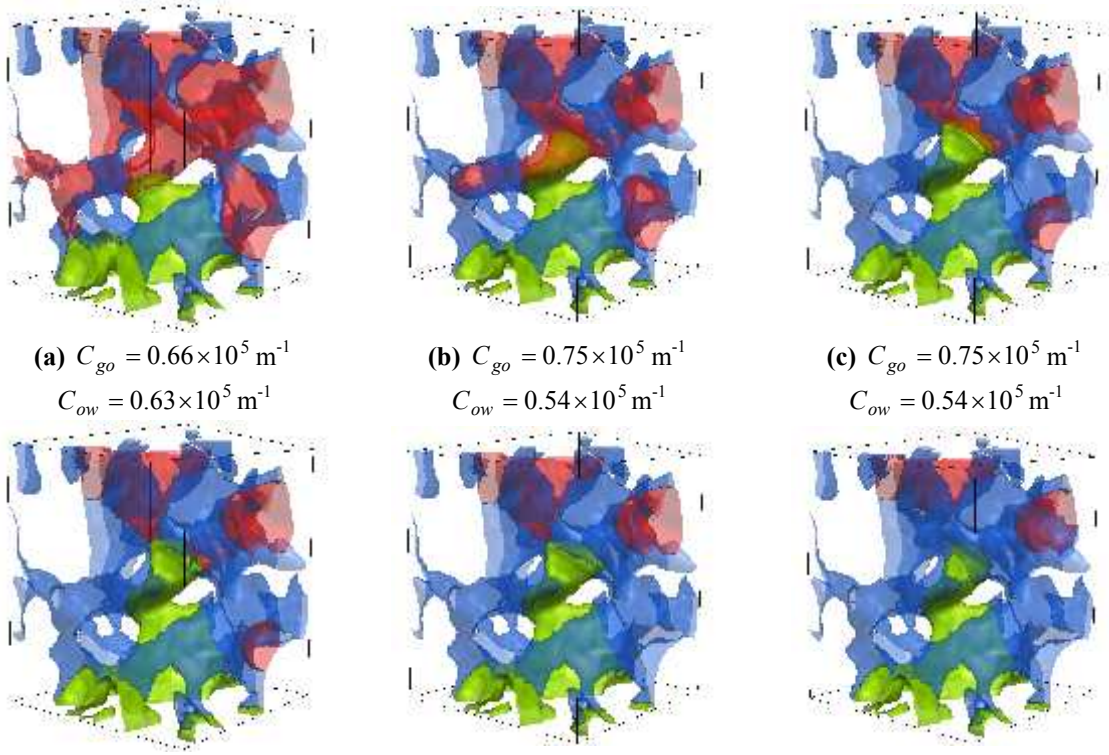

(a) $C_{go} = 0.66\times10^{5}$ m^{-1} $C_{ow} = 0.63\times10^{5}$ m^{-1} **(b)** $C_{go} = 0.75\times10^{5}$ m^{-1} $C_{ow} = 0.54\times10^{5}$ m^{-1} **(c)** $C_{go} = 0.75\times10^{5}$ m^{-1} $C_{ow} = 0.54\times10^{5}$ m^{-1}

(d) $C_{go} = 0.84\times10^{5}$ m^{-1} $C_{ow} = 0.45\times10^{5}$ m^{-1} **(e)** $C_{go} = 0.84\times10^{5}$ m^{-1} $C_{ow} = 0.45\times10^{5}$ m^{-1} **(f)** $C_{go} = 0.84\times10^{5}$ m^{-1} $C_{ow} = 0.45\times10^{5}$ m^{-1}

Figure 7: Stable (a, c and f) and unstable (b, d and e) three-phase configurations of gas (green), oil (red) and water (blue) in Castlegate sandstone for three combinations of gas-oil and oil-water capillary pressure during SWAG invasion from $S_{wi} = 0.13$ after primary drainage.

Figure 6 shows fluid configurations during the SWAG process from $S_{wi} = 0.06$. Gas displaces oil by piston-like invasion and Haines jumps as in the pure gas invasion processes in Figure 5. Simultaneously, water layers grow and eventually snap-off occurs

at the gas/oil interfaces, see for example the throats located in the lower front part of the sample in Figure 6. Figure 7 shows configurations during the SWAG process from $S_{wi} = 0.13$. Figure 7a-b shows that a three-phase water snap-off event occurs in the left part of the sample, while water snaps off oil in the right part. Figure 7c-d shows that water layers grow near the main gas/oil menisci at the top, and eventually gas/oil/water triple lines form. Figure 7d-e shows that water snaps off oil to the right, and in Figure 7e-f, three-phase water snap-off occurs at the left gas/oil interface. These events divert oil to the sides, while gas retracts downwards when water separates gas and oil completely.

CONCLUSION

We developed a three-dimensional, three-phase variational level set method for capillary-controlled displacement which accounts for a static solid phase and all permissible sets of three-phase contact angles and interfacial tensions. Simulations of three-phase capillary entry pressures for gas invasion into idealized pore throats, initially occupied by oil and water, agree excellently with analytical calculations based on (three-phase) MS-P method. The VLS method captures very well the motion of gas/oil/water triple lines and wetting-phase cusps at the triple lines, whereas oil-layer displacements in pore corners require high resolution to be modelled accurately. The next step in the development is to include volume preservation of isolated fluid clusters surrounded by one or more fluids.

We applied the VLS method on a small water-wet sandstone geometry to simulate gas- and SWAG-invasions from different initial water saturations after primary drainage. The obtained three-phase gas/oil and oil/water capillary pressure curves are comparable with the corresponding two-phase curves, but deviations occur due to different pore-scale displacement mechanisms. The level of three-phase gas/oil capillary pressure increases slightly with initial water saturation because narrow throats occupied by water prohibit invasion of gas which instead displaces oil in other locations. However, the presence of water layers in pore corners may reduce the gas/oil capillary entry pressures in parts of the sandstone as compared to the two-phase case. Differences between two- and three-phase oil/water imbibition curves are caused by snap-off mechanisms. In the three-phase case, water snap-off occurs frequently on gas/oil interfaces due to water-cusp growth at gas/oil/solid contact lines. This mechanism is observed to occur at a higher oil/water capillary pressure than the standard two-phase snap-off events in which cusps are absent.

Finally, the developed three-phase VLS method shows potential to boost interest and add applicability areas to Digital Rock Physics Technology as it need not be limited to investigating two-phase processes.

ACKNOWLEDGEMENTS

Financial support was provided by the Research Council of Norway (PETROMAKS2) through grant “234131 – Three-Phase Capillary Pressure, Hysteresis and Trapping in Mixed-Wet Rock”, and ConocoPhillips and the Ekofisk co-venturers, including TOTAL, ENI, Statoil and Petoro.

REFERENCES

1. Al-Dhahli, A., *et al.*, 2012: *Three-phase pore-network modelling for reservoirs with arbitrary wettability*, SPE-147991-PA, SPE J 18 (2), 285-295.
2. Al-Mansoori, S., *et al.*, 2009: *Three-phase measurements of non-wetting phase trapping in unconsolidated sand packs*, SPE 123994 presented at 2009 SPE ATCE, New Orleans, LA, Oct 4-7.
3. Esedoglu, S., and Smereka, P., 2008: *A variational formulation for a level set representation of multiphase flow and area preserving curvature flow*, Comm. Math. Sci. 6, 125-148.
4. Jettestuen, E., *et al.*, 2013: *A level set method for simulating capillary-controlled displacements at the pore scale with nonzero contact angles*, Water Resour. Res. 49 (8), 4645-4661.
5. Land, C, 1968: *Calculation of imbibition relative permeability for two- and three-phase flow from rock properties*, SPE Journal, Trans. AIME 243, 149-156.
6. Lenhard, R. J., and Parker, J. C., 1988: *Experimental validation of the theory of extending two-phase saturation-pressure relations to three-fluid phase systems for monotonic drainage paths*, Water Resour. Res. 24(3), 373-380.
7. Lomeland, F and Ebeltoft, E., 2013: *Versatile three-phase correlations for relative permeability and capillary pressure,* paper SCA2013-034 presented at 2013 SCA Symposium, Napa Valley, CA, USA, Sept. 16-19.
8. Mason, G., Morrow, N., 1994: *Effect of contact angle on capillary displacement curvatures in pore throats formed by spheres*, J. Colloid Interf. Sci. 168, 130-141.
9. Osher, S. and Fedkiw, R., 2002: *The level set method and dynamic implicit surfaces*, Springer-Verlag, New York.
10. Prodanović, M. and Bryant, S., 2006: *A level set method for determining critical curvatures for drainage and imbibition*, J. Colloid Interf. Sci. 304, 442-458.
11. Spiteri, E. and Juanes, R., 2006: *Impact of relative permeability hysteresis on the numerical simulation of WAG injection*, J. Petrol. Sci. Eng. 50, 115-139.
12. Svadlenka, K., Ginder, E., Omata, S, 2014: *A variational method for multiphase volume-preserving interface motions*, J. Comput. App. Math. 257, 157-179.
13. van Dijke, M. I. J., Sorbie, K. S., 2002: *The relation between interfacial tensions and wettability in three-phase systems: consequences for pore occupancy and relative permeability*, J. Petrol. Sci. Eng. 33, 39–48.
14. van Dijke, M. I. J., *et al.*, 2004: *Free energy balance for three fluid phases in a capillary of arbitrarily shaped cross-section: capillary entry pressures and layers of the intermediate-wetting phase*, J. Colloid Interf. Sci. 277, 184-201.
15. van Kats, F. M., Egberts, P. J. P., 1998: *Simulation of three-phase displacement mechanisms using a 2D lattice-Boltzmann model*, Transp. Porous Med. 37, 55-68.
16. Virnovsky, G. *et al.* 2004: *Three-phase capillary pressure measurements in centrifuge at reservoir conditions*, paper SCA2004-019 presented at 2004 SCA Symposium, Abu Dhabi, UAE, Oct. 5-9.
17. Zhao, H. K., Chan, T., Merriman, B., and Osher, S., 1996: *A variational level set approach to multiphase motion*, J. Comput. Phys. 127, 179-195.